



# Photocatalytic degradation of fluoranthene in soil suspension by TiO<sub>2</sub>/α-FeOOH with enhanced charge transfer capacity

Bingjie Yin<sup>1</sup> · Jingying Li<sup>1</sup> · Wei Guo<sup>1</sup> · Haoqing Dong<sup>1</sup> · Guangshan Zhang<sup>1</sup> · Yanjun Xin<sup>1</sup> · Guodong Zhang<sup>1,2</sup> · Qinghua Chen<sup>1</sup>

Received: 17 November 2023 / Accepted: 12 February 2024 / Published online: 21 February 2024  
© The Author(s), under exclusive licence to Springer-Verlag GmbH Germany, part of Springer Nature 2024

## Abstract

Polycyclic aromatic hydrocarbons (PAHs) in soil are potentially harmful to human health. However, the use of photocatalysis technology to treat soil contaminated with PAHs remains challenging. Therefore, TiO<sub>2</sub>/α-FeOOH composite photocatalyst has been synthesized by hydrothermal method and sol–gel method and applied to photocatalytic degradation of fluoranthene in soil. The morphology, elements, crystal structure, optical properties, electrochemical characteristics, and photocatalytic activity of TiO<sub>2</sub>/α-FeOOH have been characterized. Results showed that TiO<sub>2</sub> is tightly fixed on the surface of α-FeOOH, and TiO<sub>2</sub>/α-FeOOH had higher photocatalytic activity on photocatalytic degradation of fluoranthene in soil under simulated sunlight. The degradation efficiency of TiO<sub>2</sub>/α-FeOOH is 3.0 and 4.8 times higher than that of TiO<sub>2</sub> and α-FeOOH, respectively. This is attributed to enhanced photocatalytic ability by enhancing the transfer capacity of electrons and holes and broadening the spectrum absorption range. The highest degradation efficiency was achieved when the pH of the soil is neutral, the ratio of water/soil is 10:1, and the dosage of catalyst is 50 mg/g. In addition, it was proved that •O<sub>2</sub><sup>-</sup>, h<sup>+</sup>, and <sup>1</sup>O<sub>2</sub> are the main active substances in the photocatalysis of TiO<sub>2</sub>/α-FeOOH. The possible mechanism of a Z-type electron transfer structure was also proposed. The degradation products of fluoranthene were detected, and the degradation pathway was deduced.

**Keywords** Fluoranthene · Photocatalytic degradation · Soil suspension · Mechanism · Charges transfer capacity

## Introduction

Polycyclic aromatic hydrocarbons (PAHs) are persistent pollutants, which are mainly produced by human activities (Sun et al. 2022). Due to their toxicity, mutagenicity, and carcinogenicity, the study on the removal of PAHs is of great significance in environmental pollution control. Studies have shown that soils bear more than 90% of the environmental load of PAHs (Kariyawasam et al. 2022). These PAHs are highly toxic and biocumulative and can remain in the soil

for a long time, which can enter the human body through respiration, ingestion, skin contact, etc. These PAHs entering the human body produce toxic intermediate products after human metabolism and produce irreversible damage to macromolecular organic matter in the cell. Therefore, it is of great significance to find a method to remediate soil polluted by PAHs.

Various biological and physicochemical technologies such as adsorption, membrane filtration, aerobic/anaerobic digestion, and advanced oxidation technology are widely used for the removal of various pollutants (Jaffari et al. 2021). Of which, advanced oxidation technology is characterized by the generation of strong oxidizing hydroxyl radicals, including photocatalytic technology, Fenton oxidation technology, and ozone technology. The application of the Fenton technology is limited because it requires a low pH to achieve high efficiency. Ozone is a very powerful oxidizing agent, but it needs a high concentration dosage, and the cost is relatively high. Photocatalytic technology can utilize solar energy to degrade persistent organic pollutants (Zhang et al. 2023). It has some advantages, such as using natural

Responsible Editor: Sami Rtimi

✉ Qinghua Chen  
qhchen@qau.edu.cn

<sup>1</sup> College of Resources and Environment, Qingdao Agricultural University, Qingdao Engineering Research Center for Rural Environment, Qingdao, P. R. China

<sup>2</sup> Academy of Dongying Efficient Agricultural Technology and Industry On Saline and Alkaline Land in Collaboration With, Qingdao Agricultural University, Dongying 257029, P. R. China

energy, low cost, and high physical stability (Saravanan et al. 2022). By summarizing previous studies (Yang et al. 2023), it can be concluded that there are two main factors limiting the photocatalytic degradation efficiency of PAHs in soil. Firstly, the soil is a non-fluid medium; therefore, the mass transfer of PAH molecules in the soil is limited, thus preventing contact between PAH molecules and the photocatalyst, resulting in low photocatalytic degradation efficiency. Secondly, the penetration of light in soil is very limited, only about 0.5 mm, so the application of photocatalytic degradation technology in solid soil is greatly limited. Our research group has carried out a preliminary study on the photocatalytic degradation of PAHs in soil, and the results have shown that the degradation efficiency is only about 40% for solid phase soil under 48 h of illumination, using  $\text{TiO}_2$  (P25, 20%) as catalyst, 6 W ultraviolet lamp as light source, and fluoranthene concentration of 40 mg/kg.

Photocatalyst plays an important role in pollutant degradation and efficient utilization of solar energy.  $\text{TiO}_2$  is an environmentally friendly and inexpensive semiconductor photocatalyst, which has been widely used to degrade organic pollutants (Lam et al. 2021). Wang et al. (2016) used  $\text{TiO}_2$  with nanoscale to photocatalytic oxidize of diphenyl in soil, and the degradation rate reached 82.7% under a certain light intensity and irradiation of 3 h. However,  $\text{TiO}_2$  has two major defects, which limit its photocatalytic efficiency. On the one hand,  $\text{TiO}_2$  has a narrow spectral response range, which only accounts for 5% of the solar spectrum (Chen et al. 2016). On the other hand, the photogenerated carriers of  $\text{TiO}_2$  have high recombination efficiency. Therefore, researchers have applied a variety of methods to improve the performance and application potential of  $\text{TiO}_2$  photocatalysts. Zhao et al. prepared  $\text{TiO}_2$ @montmorillonite composite photocatalyst by combining  $\text{TiO}_2$  with montmorillonite and applied it to degrade gamma-hachloro-cyclohexane in soil. The degradation rate increased up to 70% (Zhao et al. 2007). Yong et al. (2022) synthesized  $\text{Bi}_2\text{WO}_6$  and ZnO, and the addition of  $\text{Bi}_2\text{WO}_6$  increased the visible light response range of the composite photoanode. The maximum power density of  $\text{Bi}_2\text{WO}_6/\text{ZnO}$  for treating urban sewage was  $2.707 \mu\text{W}/\text{cm}^2$ , which is 1.8 times that of pure ZnO.

Fe-containing catalysts have attracted continuous attention in the field of environmental purification due to their advantages of low toxicity, environmental friendliness, and low price (Wang et al. 2022). Fe-containing catalysts are a popular semiconductor photocatalyst used for environmental pollution control because of its narrow band gap energy, which allows an efficient visible light response (Xu and Schoonen 2000). They were widely used in the treatment of phenolic pollutants (Qian et al. 2017; Wang et al. 2017), p-chloro-nitrobenzene (Li et al. 2015), dye (Liu et al. 2017), and so on. Guo et al. (2020) prepared a Z-type  $\alpha\text{-FeOOH}/$

$\text{FeS}_2$  composite photocatalyst by hydrothermal method and applied it to Cr(VI) reduction and tetracycline degradation. Jaffari et al. synthesized Pd-loaded  $\text{BiFeO}_3$  (BFO) nanocomposites using a two-step hydrothermal method, and the composite catalysts were used to degrade malachite green dye and phenol under visible light. The results indicated that the photocatalytic performance of this microcomposite material is higher than that of BFO or commercial  $\text{TiO}_2$  (Jaffari et al. 2020). Yang et al. prepared  $\text{g-C}_3\text{N}_4/\alpha\text{-Fe}_2\text{O}_3$  by calcination of uniformly mixed ferric nitrate and  $\text{g-C}_3\text{N}_4$ , and  $\text{g-C}_3\text{N}_4/\alpha\text{-Fe}_2\text{O}_3$  was applied to photocatalytic degradation of fluoranthene in soil. Under simulated sunlight, the degradation rate reached 88.7% (Yang et al. 2023). Lam et al. applied  $\text{Ti}_3\text{C}_2$  MXene/ $\text{NiFe}_2\text{O}_4/\text{V}_2\text{O}_5$  ternary composite materials to decompose RhB, *Staphylococcus aureus*, and *Bacillus cereus*. Experiment results showed that 88.7% of RhB, 72.8% of *Staphylococcus aureus*, and 85.1% of *Staphylococcus cereus* can be degraded after 240 min of photocatalytic degradation (Lam et al. 2022).

In this work,  $\text{TiO}_2/\alpha\text{-FeOOH}$  composite photocatalyst was constructed. The morphology, elements, crystal structure, optical properties, and electrochemical characteristics of  $\text{TiO}_2/\alpha\text{-FeOOH}$  were characterized. Moreover, in order to overcome the defects of photocatalytic remediation of solid soil,  $\text{TiO}_2/\alpha\text{-FeOOH}$  was used for the degradation of fluoranthene in soil suspension. The degradation efficiency and optimal degradation conditions were investigated, and the degradation mechanism was determined.

## Experimental section

### Materials

The titanium butoxide ( $\text{C}_{16}\text{H}_{36}\text{O}_4\text{Ti}$ ) and ferrous sulfate heptahydrate ( $\text{FeSO}_4 \cdot 7\text{H}_2\text{O}$ ) were purchased from Sinopharm Chemical Reagent Co., Ltd. The rhodamine B (RhB) and fluoranthene were purchased from Aladdin Industrial Corporation. The acetic acid was purchased from Tianjin Dingshengxin Chemical Co., Ltd. The anhydrous ethanol was purchased from Yantai Sanhe Chemical Reagent Co., Ltd. The physical and chemical properties of soil are shown in Table S1.

### Preparation

#### Synthesis of $\text{TiO}_2$

$\text{TiO}_2$  powder was prepared using the sol–gel method. Twelve milliliters of  $\text{C}_{16}\text{H}_{36}\text{O}_4\text{Ti}$  and 20 mL of anhydrous ethanol were taken and mixed well. While stirring the mixture strongly, 20 mL of acetic acid aqueous solution was slowly added. The solution was left for 24 h before being dried at

105 °C. The white powder obtained after drying was ground and then calcined in a muffle furnace for 2 h to get the  $\text{TiO}_2$  powder.

### Preparation of $\alpha$ -FeOOH

The  $\alpha$ -FeOOH was synthesized by reacting a specific amount of  $\text{FeSO}_4 \cdot 7\text{H}_2\text{O}$  in an aqueous solution within a polytetrafluoroethylene reactor at 160 °C for 3 h. Afterward, the product was washed with ethanol and water and placed in a vacuum-drying oven to dry.

### Preparation of $\text{TiO}_2/\alpha$ -FeOOH

Twelve milliliters of  $\text{C}_{16}\text{H}_{36}\text{O}_4\text{Ti}$  and 20 mL of anhydrous ethanol were mixed, and then 20 mL of acetic acid solution was added into the mixture and stirred for 30 min. After leaving the mixture for 24 h,  $\text{TiO}_2$  gel was formed. The  $\text{TiO}_2$  gel was diluted, and  $\alpha$ -FeOOH (Fe: Ti = 1:4, mol/mol) was added to the mix. The optimization process was illustrated in Fig. S1. The reaction system was stirred for 2 h at 60 °C. After drying for 12 h at 80 °C,  $\text{TiO}_2/\alpha$ -FeOOH was obtained. The resultant route is represented in Fig. 1.

### Characterization

The scanning electron microscopy (SEM, ZEISS Gemini 300) and transmission electron microscope (TEM, Jem2100) equipped with energy dispersive spectroscopy (EDS) provided the morphology and structure of the samples. The Raman spectrum was recorded by a Raman spectrometer (HORIBA Scientific LabRAM HR Evolution). X-ray photoelectron spectroscopy (XPS) measurement was conducted using a Thermo Fisher ESCALAB XI<sup>+</sup>. The crystalline structure of the samples was measured by an X-ray diffractometer (XRD). The light absorption properties of the samples were studied by UV–Vis DRS (Shimadzu 2600).

Fourier transform infrared spectroscopy (FTIR) spectra were recorded by Thermo Scientific Nicolet iS20. Specific surface area analysis was performed by Micromeritics ASAP 2460 automatic pore analyzer. The CHI660E electrochemical workstation was used for the photoelectric chemical detection, and the standard three-electrode system was adopted. The prepared  $\text{TiO}_2/\alpha$ -FeOOH was coated on the conductive glass as the working electrode, the platinum electrode was used as the opposite electrode, and the silver-silver chloride electrode was used as the reference electrode. PL was detected by an F-4700 fluorescence spectrometer at an excitation wavelength of 315 nm and emission wavelength of 425 nm.

### Photocatalytic activity

#### Soil pretreatment

The test soil was firstly dried and grinded and then passed it through a 1-mm screen. The obtained soil sample was treated by high-temperature sterilization for 2 times (121 °C, 0.5 h). After drying, 100 mL of a mixture of methylene chloride and acetone with a volume ratio of 1:1 was added to 100 g of soil, ultrasonic cleaning for 30 min, then, the supernatant was discarded after static settlement. This operation process was repeated for 3 times. Then, the soil was dried for use.

#### Preparation of contaminated soil

The fluoranthene-contaminated soil samples with a concentration of 40 mg/kg were obtained by adding fluoranthene-methanol solution into the pre-treated soil and mixing thoroughly. Then, the samples were volatilized to remove methanol.

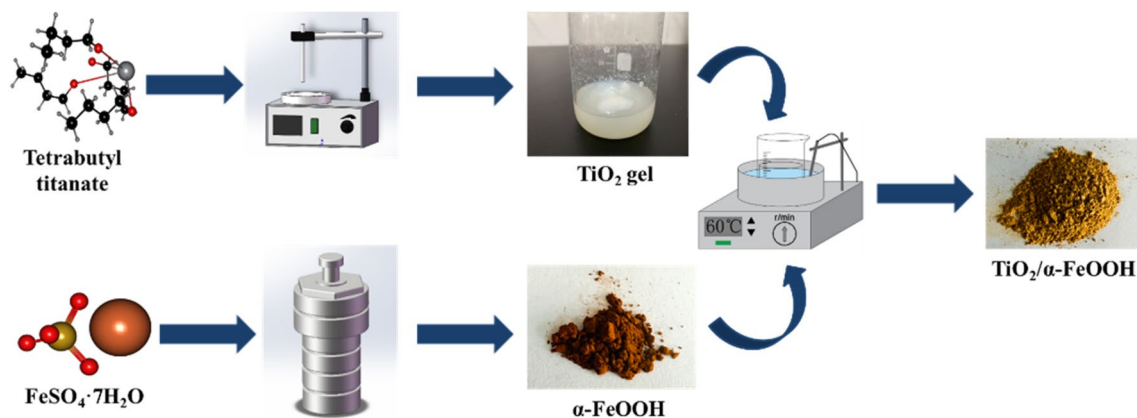


Fig. 1 Synthesis route of  $\text{TiO}_2/\alpha$ -FeOOH

## Photocatalytic performance test

Photocatalytic experiments were conducted in a photocatalytic reactor. Rhodamine B (RhB) was chosen as an indicative contaminant for rapid evaluation of the catalytic performance of catalysts. RhB solution (100 mL, 5 mg/L) and 20 mg photocatalyst were added into a beaker and stirred with a magnetic stirrer. After equilibrium of adsorption and desorption for 1.5 h, a 35-W Xenon lamp was used to illuminate the reactive solution, and the distance between the light source and the reaction solution was 12 cm. The irradiation time was 2 h. Taking 5 mL of solid–liquid mixture every 30 min during the illumination period to centrifugal separation (4000 r/min) for 5 min and collecting liquid supernatant to measure the concentration of RhB.

## Photocatalytic degradation of fluoranthene in soil

Soil-containing fluoranthene (40 mg/kg) was mixed with water in a certain proportion (1:1, 5:1, 10:1, 15:1, 20:1, water/soil = w/w) to form a soil suspension (soil-containing fluoranthene was aged at room temperature for 2 months). Photocatalyst was added into the soil suspension, and a 35-W xenon lamp was used as the light source with a 12 cm distance from the soil suspension. After centrifugation and desiccation, fluoranthene was extracted with organic solvent and purified by a solid phase extraction column. The concentration of fluoranthene was determined by high-performance liquid chromatography (HPLC) after spin evaporation, constant volume, and filtration (the concentration of fluoranthene in the supernatant is almost zero and has no effect on the results).

The detailed detection methods: adding 10 mL of acetone-n-hexane solution (1:1, v/v) into the dried soil. After mixing, ultrasonic treatment for 30 min. Then, the mixture was centrifuged at a speed of 4000 r/min for 10 min, and the supernatant was retained. Five milliliters of supernatant was purified by chromatography column (4 g silica gel + 2 g anhydrous sodium sulfate). The purification procedure was as follows: firstly, 20 mL dichloromethane was added to activate the silica gel column; then, 5 mL supernatant was added into the column; finally, 20 mL acetone-n-hexane solution (1:1, v/v) was used to elute fluoranthene from extraction column, and the eluent was collected. The eluent was evaporated by a rotary evaporator to near drying; after that, the eluent was dissolved with 2 mL of methanol. The concentration of fluoranthene was measured by HPLC after filtration with a 0.22- $\mu$ m filter membrane. Liquid phase detection conditions: C18 chromatographic column (4.6 mm  $\times$  250 mm), mobile phase (95% methanol + 5% ultra-pure water), UV detector with detector wavelength 324 nm. The adding standard recovery was  $90 \pm 5\%$ . Accuracy of the detection method was 3%.

## Active species trapping

In order to reveal the possible degradation mechanism, the active species in the photocatalytic reaction were identified by free radical scavenging tests. P-benzoquinone (BQ, 10 mg) was used as the quenching agent of superoxide radical ( $\cdot\text{O}_2^-$ ), tert-butanol (TBA, 5 mL) was used as the quenching agent of hydroxyl radical ( $\cdot\text{OH}$ ), potassium iodide (KI, 250 mg) was used as the quenching agent of hole ( $h^+$ ), and tetramethylpiperidine (TEMPOL, 20 mg) was used as the quenching agent of singlet oxygen ( $^1\text{O}_2$ ). By comparing the change of degradation rate before and after adding the quenching agent, the active free radicals in the reaction process were qualitatively analyzed.

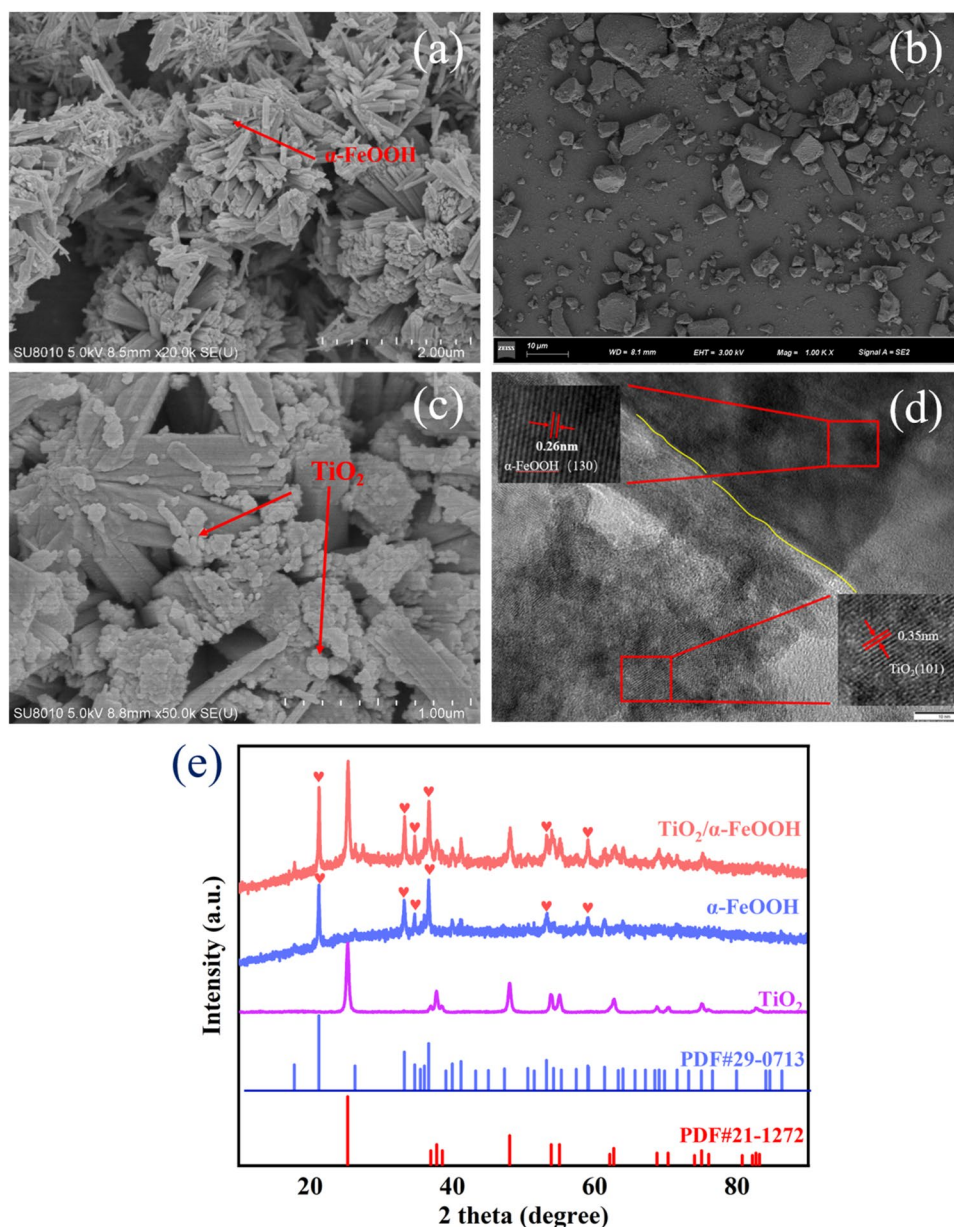
## Results and discussion

### Characterization of photocatalysts

The structural characteristics and general morphology of  $\text{TiO}_2/\alpha\text{-FeOOH}$  were analyzed by SEM and TEM. As shown in Fig. 2a, b,  $\alpha\text{-FeOOH}$  presents a needle-like structure with a diameter of about 100–200 nm and a length ranging from tens to hundreds of nanometers.  $\text{TiO}_2$  presents as a blocky structure, with a particle size in tens to hundreds of nanometers. Figure 2c is the SEM image of  $\text{TiO}_2/\alpha\text{-FeOOH}$ . It can be clearly found that a large number of  $\text{TiO}_2$  NPs are anchored on the surface of  $\alpha\text{-FeOOH}$ , and the surface of  $\alpha\text{-FeOOH}$  becomes rough. Further, high-resolution TEM (HRTEM) was used to ascertain the coupling of  $\alpha\text{-FeOOH}$  and  $\text{TiO}_2$ . As can be seen from Fig. 2d, lattice fringes with crystal plane spacing of 0.35 nm are consistent with the (101) plane of anatase  $\text{TiO}_2$ , and the lattice spacing of 0.26 nm can be well attributed to the (130) crystal plane of  $\alpha\text{-FeOOH}$ . It is also noted that  $\text{TiO}_2$  is in close contact with  $\alpha\text{-FeOOH}$ , and a clear interface can be observed between the  $\text{TiO}_2$  and  $\alpha\text{-FeOOH}$ . These results demonstrate the successful recombination of  $\text{TiO}_2$  and  $\alpha\text{-FeOOH}$ .

The XRD patterns of pure  $\text{TiO}_2$ ,  $\alpha\text{-FeOOH}$ , and  $\text{TiO}_2/\alpha\text{-FeOOH}$  samples are shown in Fig. 2e. The diffraction peaks at  $\theta = 25.4^\circ$ ,  $37.8^\circ$ ,  $48.1^\circ$ ,  $53.9^\circ$ ,  $62.9^\circ$ , and  $70.5^\circ$  can be well assigned to the typical (101), (004), (200), (105), (204), and (220) crystal planes of anatase  $\text{TiO}_2$  (JCPDS, NO.21–1272), and the crystallize size of  $\text{TiO}_2$  is 23.6 nm. For  $\alpha\text{-FeOOH}$ , all the diffraction peaks can be well belonged to the standard pattern of  $\alpha\text{-FeOOH}$  (JCPDS, no. 29–0173) (Zhao et al. 2018). The crystal size of  $\alpha\text{-FeOOH}$  is 57.8 nm. In the XRD pattern of  $\text{TiO}_2/\alpha\text{-FeOOH}$ , the characteristic peaks of  $\text{TiO}_2$  and  $\alpha\text{-FeOOH}$  appeared at the same time, indicating that two materials are well combined. Meanwhile, compared with pure  $\text{TiO}_2$  and  $\alpha\text{-FeOOH}$ , the intensity of XRD diffraction peaks of  $\text{TiO}_2/\alpha\text{-FeOOH}$  was weakened,

**Fig. 2** SEM images of **a**  $\alpha$ -FeOOH; **b**  $\text{TiO}_2$ ; **c**  $\text{TiO}_2/\alpha$ -FeOOH; **d** HRTEM image of  $\text{TiO}_2/\alpha$ -FeOOH; **e** XRD patterns of  $\text{TiO}_2$ ,  $\alpha$ -FeOOH, and  $\text{TiO}_2/\alpha$ -FeOOH

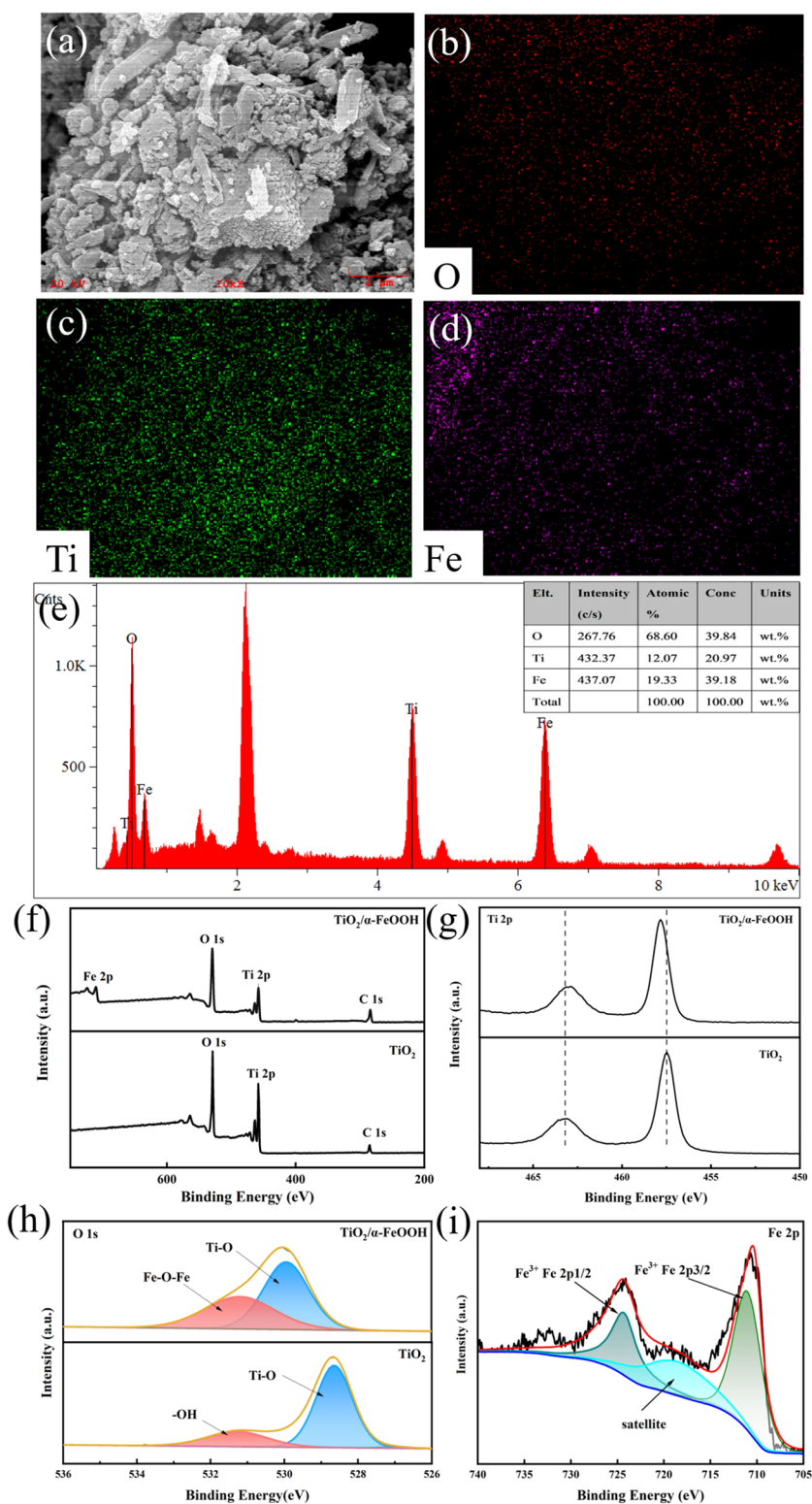


and the peak width was wider, indicating that the relative percentage content of each substance was less, and the crystalline grain size of composite material reduced after composition. Above results showed that  $\text{TiO}_2/\alpha$ -FeOOH composite photocatalyst was successfully prepared. The reduction of grain size may be beneficial to the improvement of catalyst performance. The element species and content of  $\text{TiO}_2/\alpha$ -FeOOH were determined by EDX analysis. As shown in Fig. 3b–e, the elements of O, Ti, and Fe were all detected in  $\text{TiO}_2/\alpha$ -FeOOH, which further verified the above conclusions.

XPS was used to further determine the components' composition and valence states of  $\text{TiO}_2/\alpha$ -FeOOH photocatalyst. The XPS measurement spectrum (Fig. 3f) exhibits

the presence of Fe, O, and Ti elements in  $\text{TiO}_2/\alpha$ -FeOOH and Ti and O elements in  $\text{TiO}_2$ . In addition, the chemical valence states of Fe, O, and Ti elements were analyzed by high-resolution XPS spectroscopy, and the spectra of Ti 2p, O 1s, and Fe 2p were shown in Fig. 3g–i. In Fig. 3g, the peaks at 463.0 eV and 457.5 eV correspond to Ti 2p<sub>1/2</sub> and Ti 2p<sub>3/2</sub> of  $\text{TiO}_2$ , respectively. The distance between the two peaks is 5.5 eV, indicating that the valence state of Ti is  $\text{Ti}^{4+}$ . Compared with  $\text{TiO}_2$ , the Ti 2p<sub>1/2</sub> and Ti 2p<sub>3/2</sub> peaks of  $\text{TiO}_2/\alpha$ -FeOOH are slightly positively shifted, resulting in a decrease in binding energy, which may be due to the change in electron cloud density caused by electronic interaction between  $\text{TiO}_2$  and  $\alpha$ -FeOOH. These results suggest that the composites are connected

**Fig. 3** a–d Element mapping images and e EDX image of  $\text{TiO}_2/\alpha\text{-FeOOH}$ ; XPS spectra of  $\text{TiO}_2$  and  $\text{TiO}_2/\alpha\text{-FeOOH}$ : f full survey spectrum; g Ti 2p; h O 1s; i Fe 2p



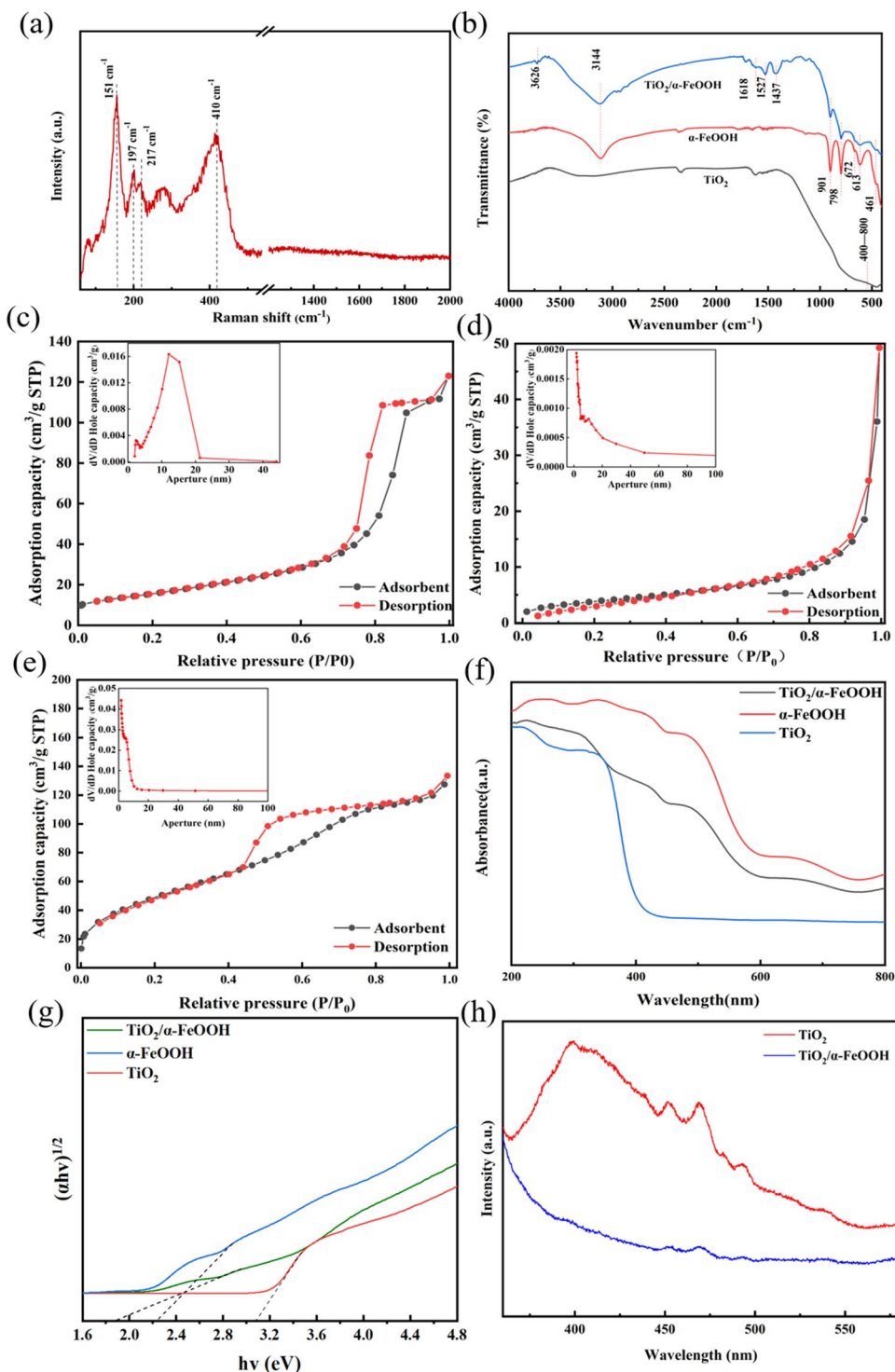
by chemical bonds rather than physical mixing. Figure 3 h is a fine spectrum of O 1s, where the characteristic peaks at 528.6 eV and 531.1 eV of  $\text{TiO}_2$  correspond to Ti–O and surface hydroxyl. For the  $\text{TiO}_2/\alpha\text{-FeOOH}$ , 529.9 eV corresponds to Ti–O, and the characteristic peak at 531.1 eV

corresponds to Fe–O–Fe (Huang et al. 2018; Rajender et al. 2018). Figure 3i presents the high-resolution XPS spectra of Fe 2p; the characteristic peak at 724.6 eV is attributed to Fe 2p<sub>1/2</sub>, and 711.1 eV corresponded to Fe 2p<sub>3/2</sub>, which belongs to  $\text{Fe}^{3+}$  ion (Xie et al. 2013). In addition,

the satellite peak of Fe at 719.0 eV may be caused by the energy loss after the valence band electrons transition to the conduction band. From these results, it can be inferred that TiO<sub>2</sub>/α-FeOOH heterostructure is formed through interface contact between TiO<sub>2</sub> and α-FeOOH, which could enhance electron interactions by offering fast electron-transfer channels.

To further confirm the presence of TiO<sub>2</sub> and α-FeOOH, the samples were analyzed using Raman spectroscopy. As shown in Fig. 4a, the characteristic bands at 144 and 198 cm<sup>-1</sup> are assigned to TiO<sub>2</sub> crystalline phase; meanwhile, the strong feature band detected at 410 cm<sup>-1</sup>, and the feature peak at 215 cm<sup>-1</sup> corresponds to α-FeOOH (Wei et al. 2017; Wu et al. 2023; Pant et al. 2019; Cao et al. 2016; Cizmar

**Fig. 4** **a** Raman spectrum of TiO<sub>2</sub>/α-FeOOH and **b** FTIR spectra of TiO<sub>2</sub>/α-FeOOH; adsorption–desorption isotherm curves of **c** TiO<sub>2</sub>, **d** α-FeOOH, and **e** TiO<sub>2</sub>/α-FeOOH; UV–vis diffuse reflectance absorption spectra (**f**) and plots of (αhm)<sup>1/2</sup> vs photon energy (hm) (**g**) of TiO<sub>2</sub>, α-FeOOH, and TiO<sub>2</sub>/α-FeOOH; PL spectra (**h**) for TiO<sub>2</sub> and TiO<sub>2</sub>/α-FeOOH



et al. 2020). The presence of these characteristic peaks further confirms the successive construction of  $\text{TiO}_2/\alpha\text{-FeOOH}$  composite. The FTIR spectrum of  $\text{TiO}_2/\alpha\text{-FeOOH}$  was used to verify the chemical bonding and compositions, as shown in Fig. 4b. The characteristic peaks at 3144, 901, 798, and  $461\text{ cm}^{-1}$  are caused by the tensile vibration of O–H (Liu et al. 2017), bending vibration of Fe–O–H (Rahimi et al. 2015), and Fe–O tensile vibration in  $\alpha\text{-FeOOH}$  (Xie et al. 2013; Zhang et al. 2013), respectively. In addition, the characteristic peak of  $\text{TiO}_2$  at  $461\text{ cm}^{-1}$  corresponds to the wide absorption peak of Ti–O and Ti–O–Ti. The absorption peak formed at  $1437\text{ cm}^{-1}$  is due to the bonding between  $\text{TiO}_2$  and  $\alpha\text{-FeOOH}$  (Magalhães et al. 2004). Two peaks at 1618 and  $3626\text{ cm}^{-1}$  correspond to vibrations of adsorbed water and oxygen in the hydroxyl group (Karimi Sahnesarayi et al. 2014), respectively. In addition, due to the interaction between  $\text{TiO}_2$  and  $\alpha\text{-FeOOH}$  charge, the absorption peak of the composite material is enhanced (Cao et al. 2016).

The pore structure and specific surface area of catalysts are important factors affecting their catalytic activity. The adsorption-desorption isotherms and surface areas of  $\text{TiO}_2$ ,  $\alpha\text{-FeOOH}$ , and  $\text{TiO}_2/\alpha\text{-FeOOH}$  were determined by the nitrogen adsorption method. As shown in Fig. 4c,  $\text{TiO}_2$  is a type III adsorption isotherm with an H1-type hysteresis loop. This indicates that  $\text{TiO}_2$  has a large pore structure, and the interaction force is strong; moreover, the pore size distribution is relatively uniform (Zhang et al. 2019).  $\alpha\text{-FeOOH}$  also belongs to type III adsorption isotherms (Fig. 4d), but is H3 hysteresis loops, indicating that the pore structure of  $\alpha\text{-FeOOH}$  is irregular (Liu et al. 2021). From Fig. 4e, it can be found that  $\text{TiO}_2/\alpha\text{-FeOOH}$  composite shows type II adsorption isotherms and H2 hysteresis loops, indicating the presence of mesoporous structures, which are complex and often found in ordered mesoporous materials after hydrothermal treatment (Sultan et al. 2018). The specific surface areas of  $\text{TiO}_2$ ,  $\alpha\text{-FeOOH}$ , and  $\text{TiO}_2/\alpha\text{-FeOOH}$  calculated by the  $\text{N}_2$  adsorption-desorption curve (Beller) are 56.64, 14.10, and  $184.81\text{ m}^2/\text{g}$ , respectively (as shown in Table S2). The porous structure and large surface area of the material not only improve the adsorption performance but also promote the light absorption and utilization. When  $\text{TiO}_2$  is combined with  $\alpha\text{-FeOOH}$ , the specific surface area increases significantly, which means that the composite material can provide more active sites, and the probability of pollutants entering the surface and interface of the material is enhanced (Lin et al. 2019). Ultimately, the catalytic performance of the material is improved.

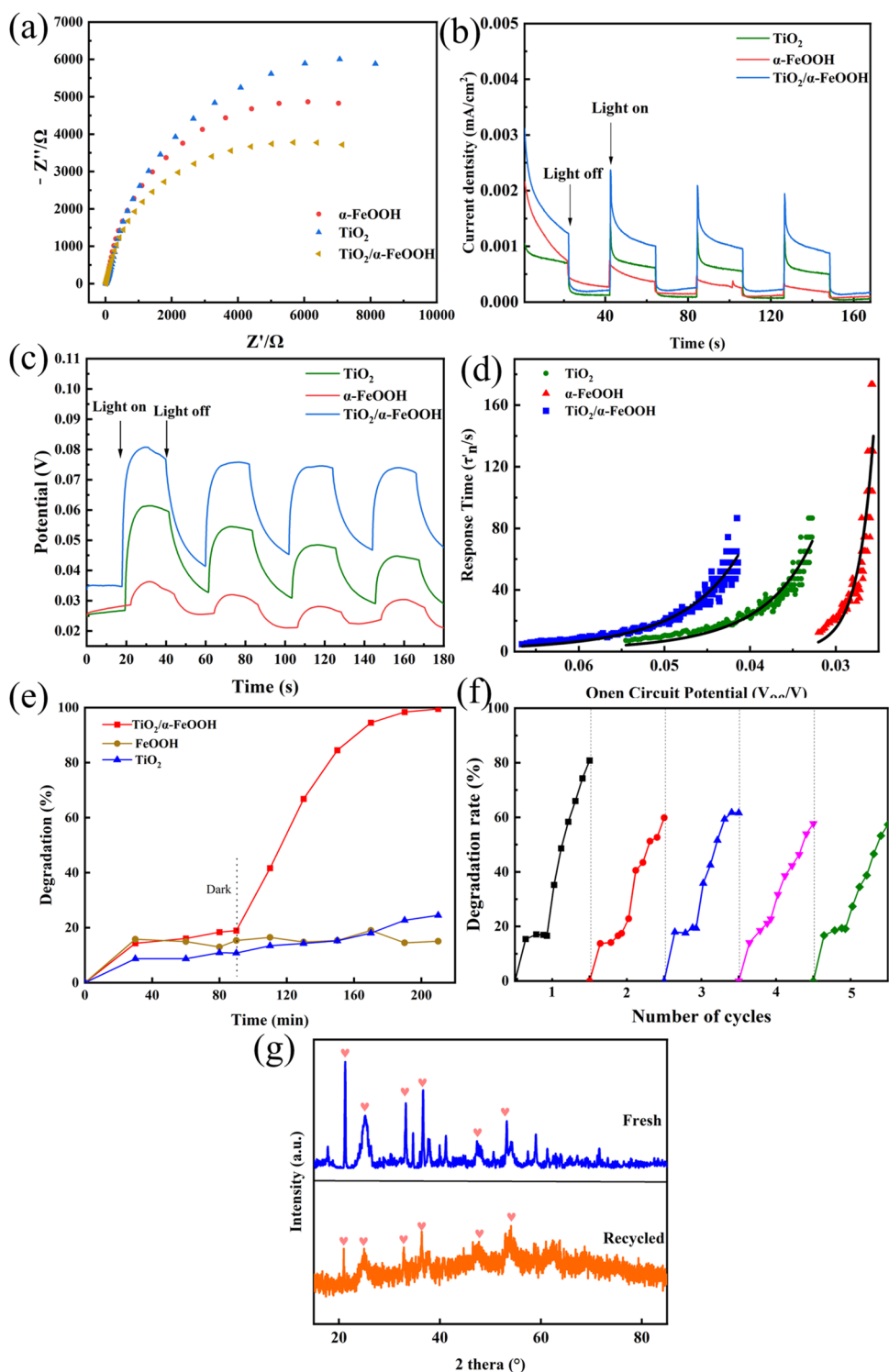
The light absorption properties of  $\text{TiO}_2$ ,  $\alpha\text{-FeOOH}$ , and  $\text{TiO}_2/\alpha\text{-FeOOH}$  were measured by UV–Vis diffuse reflection spectroscopy. As shown in Fig. 4f, pure  $\text{TiO}_2$  has very weak absorption in the visible region, while  $\alpha\text{-FeOOH}$  shows strong light adsorption in the entire ultraviolet and visible regions. The combination of  $\text{TiO}_2$  and  $\alpha\text{-FeOOH}$  obviously

improves the optical absorption capacity, particularly in the visible region, making  $\text{TiO}_2/\alpha\text{-FeOOH}$  absorb in both ultraviolet and visible region. The band gap of a semiconductor can be calculated by the Kubelka–Munk equation. The calculated bandgap energy of  $\text{TiO}_2$  and  $\alpha\text{-FeOOH}$  is 3.21 eV and 2.18 eV, respectively (Fig. 4g). After coupling  $\text{TiO}_2$  and  $\alpha\text{-FeOOH}$ , the band gap of  $\text{TiO}_2/\alpha\text{-FeOOH}$  photocatalyst becomes 2.41 eV. Results show that there is a strong interfacial interaction or contact interface between  $\text{TiO}_2$  and  $\alpha\text{-FeOOH}$ , which effectively enhances the visible light response (Ma et al. 2017). The separation efficiency of photoexcited electron–hole pairs is a key parameter directly related to the photocatalytic activity of photocatalysts. Therefore, the separation efficiency of photogenerated carriers of  $\text{TiO}_2/\alpha\text{-FeOOH}$  was evaluated by PL spectroscopy. It is well known that the lower the PL intensity, the higher the separation efficiency of electrons and holes (Liang et al. 2018). Figure 4h shows the PL spectra detected at 315 nm excitation wavelength. Low PL strength was observed after  $\text{TiO}_2$  was combined with  $\alpha\text{-FeOOH}$ , indicating that the combination of  $\text{TiO}_2$  with  $\alpha\text{-FeOOH}$  increases the separation efficiency of electrons and holes. Consequently, it can be predicted that  $\text{TiO}_2/\alpha\text{-FeOOH}$  will exhibit higher photocatalytic activity.

To further confirm the enhanced migration and separation efficiency of photogenerated carriers, a series of photoelectrochemical and electrochemical measurements were conducted. As shown in Fig. 5a, the charge transfer resistance was evaluated by electrochemical impedance spectroscopy (EIS) analysis. The diameter of semicircle in Nyquist diagram represents the information about charge transfer behavior at material interface (Ma et al. 2020). The smaller the semicircle diameter, the lower the resistance, and the faster the charge transfer rate. It is clear that the  $\text{TiO}_2/\alpha\text{-FeOOH}$  composite has a smaller semicircle diameter, indicating a smaller charge-transfer resistance and smoother charge diffusion, as well as more efficient charge separation and interfacial transfer. Moreover, the separation efficiency of photogenerated electrons-hole pairs was also evaluated by measuring the transient photocurrent density and open circuit potential ( $V_{oc}$ ). Figure 5b shows that the transient photocurrent response is very fast, indicating that the materials have good photosensitivity (Zhang et al. 2020). Meanwhile, the photocurrent density of  $\text{TiO}_2/\alpha\text{-FeOOH}$  is  $0.0032\text{ mA}/\text{cm}^2$ , which is 1.45 and 2.91 times as many as that of  $\text{TiO}_2$  ( $0.0022\text{ mA}/\text{cm}^2$ ) and  $\alpha\text{-FeOOH}$  ( $0.0011\text{ mA}/\text{cm}^2$ ), respectively.  $V_{oc}$  corresponds to the Fermi energy-level difference between the photoanode and the counter electrode and due to the accumulation of electrons, the Fermi level will shift to a more negative point position, resulting in the formation of  $V_{oc}$ . As shown in Fig. 5c,  $V_{oc}$  gradually increases after the light is turned on and remains stable after reaching a maximum, which may be due to the accumulation



**Fig. 5** Electrochemical impedance (a); photocurrent density (b); open circuit potential (c); and response time (d) of TiO<sub>2</sub>, α-FeOOH, and TiO<sub>2</sub>/α-FeOOH; (e) comparison of photocatalytic efficiency of TiO<sub>2</sub>, α-FeOOH, and TiO<sub>2</sub>/α-FeOOH; (f) stability measurement of TiO<sub>2</sub>/α-FeOOH; (g) XRD images of TiO<sub>2</sub>/α-FeOOH fresh and after five cycles



of electrons and competition from carrier recombination (Mor et al. 2013; Meekins and Kamat 2009). Obviously, TiO<sub>2</sub>/α-FeOOH exhibits a higher V<sub>oc</sub> (0.08 V) than TiO<sub>2</sub> (0.06 V) and α-FeOOH (0.035 V) photoelectrodes. These results confirm that TiO<sub>2</sub>/α-FeOOH has high photoelectric conversion ability, and coupling TiO<sub>2</sub> and α-FeOOH

improves electron–hole pair separation and electron accumulation (Sajjadizadeh et al. 2019). The electron recombination kinetics of TiO<sub>2</sub>/α-FeOOH were measured to understand the charge-transport properties. Figure 5d shows the τ<sub>n</sub> ~ V<sub>oc</sub> curve calculated by open-circuit voltage decay (OCVD). According to Buisquert, the recombination reaction response

time of the electrons was obtained by the reciprocal of derivative of the decay curve normalized by the thermal voltage (Bisquert et al. 2004, 2009; Bang and Kamat 2010).

$$\tau_n = \frac{k_B T}{e} \left( \frac{dV_{oc}}{dt} \right)^{-1}$$

where  $K_B T$  is the heat energy,  $e$  is the basic charge, and  $dV_{oc}/dt$  is the reciprocal of the transient open circuit potential. The application of this expression is to assume that the recombination of electrons is linear and occurs only in electrolyte and is first-order dependent on electron concentration. The attenuation of open circuit potential after irradiation interruption reflects the decrease of electron concentration. The recombination rate of photoelectrons is directly proportional to the response of OCVD (Yu et al. 2009; Zheng et al. 2015). From Fig. 5d, it can be observed that the electron lifetime of  $\text{TiO}_2/\alpha\text{-FeOOH}$  composite is increased compared with that of single  $\text{TiO}_2$  and  $\alpha\text{-FeOOH}$  at a given open-circuit potential of 0.03–0.055 V. These results mean that the recombination rate of photogenerated electrons is slower after coupling of  $\text{TiO}_2$  and  $\alpha\text{-FeOOH}$ , which would improve the efficiency of electron utilization and boost the photocatalytic performance.

### Measurement of photocatalytic activity and photocatalytic degradation of fluoranthene in soil

The catalytic activity and stability of the catalysts were investigated using RhB (5 mg/L) as an indicator pollutant. From Fig. 5e, it can be found that after 90 min of blank experiment under illumination, the concentration of RhB decreases by about 15%, which could be due to physical adsorption. After illumination for 120 min, the degradation efficiency of pure  $\text{TiO}_2$  and  $\alpha\text{-FeOOH}$  is only 24.52 and 15.06%, respectively. Whereas, the  $\text{TiO}_2/\alpha\text{-FeOOH}$  shows greatly enhanced photocatalytic performance with a photocatalytic degradation rate of 89.52%. This is attributed to the improved light absorption and charges-transport capacity. The stability of  $\text{TiO}_2/\alpha\text{-FeOOH}$  was investigated by 5 cycles of RhB degradation under 35-W xenon lamp irradiation. As shown in Fig. 5f, the degradation rate decreases by 19% after the first cycle and remains basically stable after four cycles. The loss of degradation efficiency is about 23% after 5 cycles, which may be due to the combination of pollutants and catalyst surface in degradation process. XRD analysis was conducted on  $\text{TiO}_2/\alpha\text{-FeOOH}$  before and after use, and the results are shown in Fig. 5g. As can be seen, the intensity of  $\text{TiO}_2/\alpha\text{-FeOOH}$  diffraction peaks decreased after five cycles, but several major XRD diffraction peaks can still be clearly observed. Furthermore, the ICP measurement

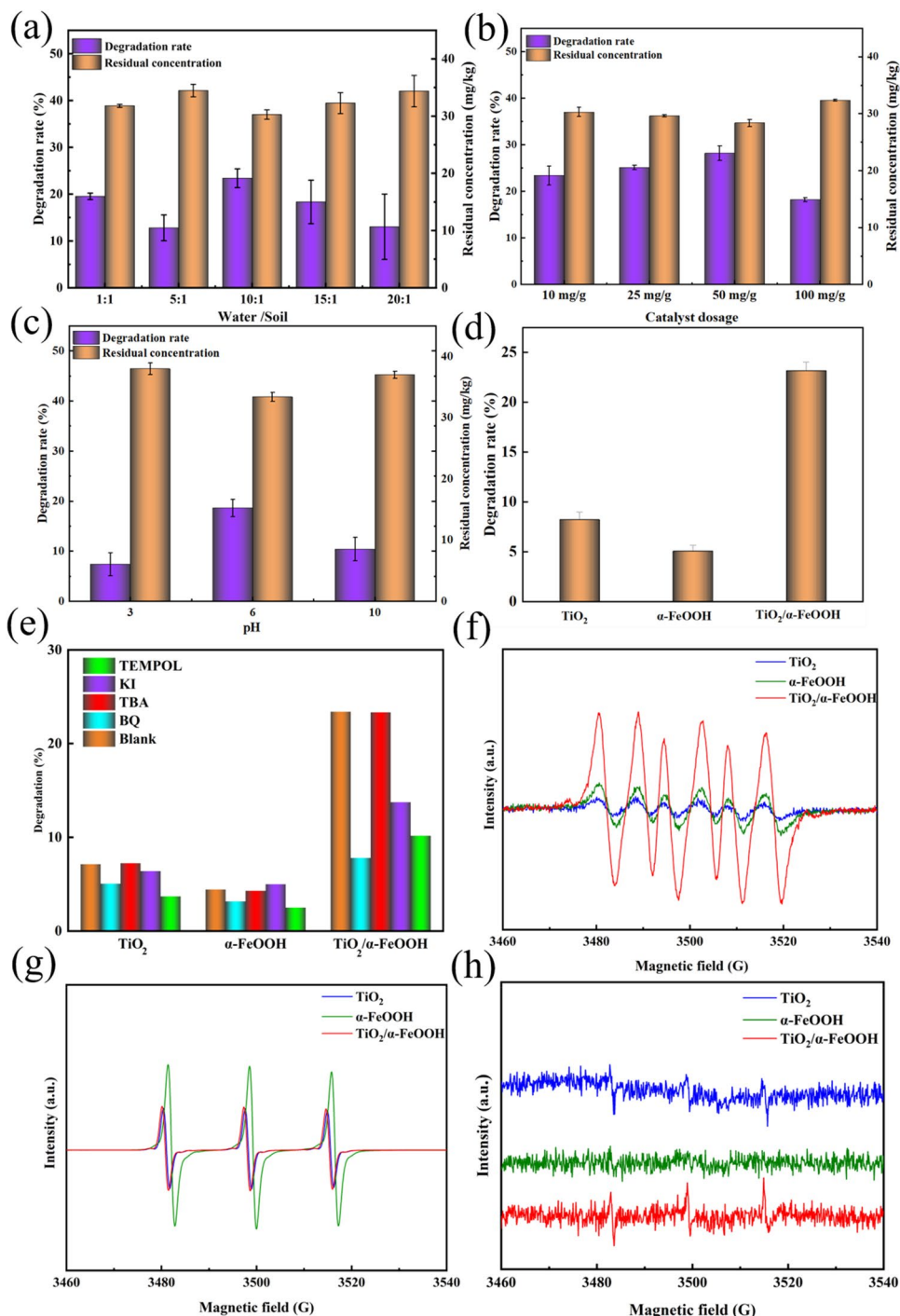
showed that Fe leaching is negligible (as shown in Table S3). These results prove that  $\text{TiO}_2/\alpha\text{-FeOOH}$  can still maintain a relatively complete crystal structure after 5 cycles.

In order to explore the degradation performance of  $\text{TiO}_2/\alpha\text{-FeOOH}$  on fluoranthene in soil, the degradation experiments were conducted under various conditions. For traditional solid-phase photocatalytic degradation of soil, limited light penetration is an important problem. Therefore, to improve the light penetration of the reaction system, water and soil with different ratios (water/soil = 1:1, 5:1, 10:1, 15:1, and 20:1) were configured to form a soil suspension system. The catalyst dosage was set as 20 mg, and the degradation rate was measured after 4 h of xenon lamp irradiation (35 W). As shown in Fig. 6a, by increasing the ratio of water/soil from 1:1 to 10:1, the degradation efficiency of fluoranthene was effectively improved, which may be because water dilutes the reaction system and increases light penetration capacity, thus enhancing the absorption of light by the catalyst. Meanwhile, the addition of water improves the mass transfer of pollutant molecules in the reaction system. In addition, more water can promote the reaction system to produce more  $\cdot\text{OH}$ , thus increases the degradation efficiency (Wang et al. 2016). However, when the ratio of water/soil is greater than 10:1, the degradation rate decreases on the contrary, which may be due to the high proportion of water in the system. Excess water causes the photocatalytic material to be in a high suspension state, which is not conducive to contact with fluoranthene molecule, leading to the decrease of degradation rate.

Catalyst dosage is an important parameter in catalytic degradation process. In order to determine the optimal dosage of photocatalyst, different doses of  $\text{TiO}_2/\alpha\text{-FeOOH}$  (10, 25, 50, 100 mg/g; photocatalyst:soil) were used to investigate the photocatalytic activity on degradation of fluoranthene in soil suspension. As shown in Fig. 6b, the degradation rate increased with the increase of catalyst dosage from 10 to 50 mg/g. This may be because more catalyst generates more electron–hole pairs, leading to more reactive free radicals (Dong et al. 2010b), thus promoting photocatalytic degradation. However, when the dosage of catalyst reached 100 mg/g, the degradation rate decreased, which may be due to the excessive photocatalyst increases the turbidity of the solution and reduces the light penetration (Gupta et al. 2012). In addition, excessive catalyst will lead to agglomeration, thus reducing the active sites of catalyst, eventually resulting in the degradation of catalyst performance (Anju et al. 2012).

The pH of soil is closely related to the chemical and mineral properties of soil such as zeta potential, cation exchange capacity, and redox potential. In order to study the effect of soil pH on the photocatalytic degradation efficiency of fluoranthene, degradation experiments were carried out under acidic (pH = 3), neutral (pH = 6), and

**Fig. 6** **a** Effect of water/soil; **b** effect of photocatalyst dosage; **c** effect of initial pH; **d** comparison of photocatalytic degradation efficiency on fluoranthene in soil of TiO<sub>2</sub>, α-FeOOH, and TiO<sub>2</sub>/α-FeOOH; **e** effect of trapping agents on degradation efficiency of TiO<sub>2</sub>, α-FeOOH, and TiO<sub>2</sub>/α-FeOOH; ESR spectra of **f** DMPO-·O<sub>2</sub><sup>-</sup>, **g** TEMPO-h<sup>+</sup>, and **h** TEMP-<sup>1</sup>O<sub>2</sub> of TiO<sub>2</sub>, α-FeOOH, and TiO<sub>2</sub>/α-FeOOH



alkaline (pH = 10) conditions, respectively, and the results were shown in Fig. 6c. Under neutral condition, the photocatalytic degradation rate (18.62%) is higher than that of acid and alkaline condition. The reason may be related with the aquatic medium surrounding the soil. Du et al. (2022) showed that the adsorption capacity of PAHs may be affected by pH of soil. The soil under neutral condition may be more conducive to the interaction between fluoranthene and catalyst, thus improving the degradation efficiency.

The photocatalytic degradation efficiency of TiO<sub>2</sub>/α-FeOOH on fluoranthene in soil suspension was compared with TiO<sub>2</sub> and α-FeOOH. As shown in Fig. 6d, the degradation rate of TiO<sub>2</sub>, α-FeOOH, and TiO<sub>2</sub>/α-FeOOH is 8.35, 5.10, and 23.18%, respectively. TiO<sub>2</sub>/α-FeOOH shows better catalytic performance than the single catalyst, which is 2.78 and 4.55 times as many as that of TiO<sub>2</sub> and α-FeOOH, respectively. This result further confirms that the coupling of TiO<sub>2</sub> and α-FeOOH improves the photocatalytic activity

obviously. Table 1 lists a comparison of various technical systems related to the degradation of pollutants in soil. As displayed, TiO<sub>2</sub>/α-FeOOH exhibits relatively higher advantages in degradation efficiency, reaction time, and reaction conditions than those reported in the literatures.

### Photocatalytic mechanism exploration

It is generally believed that the photocatalytic degradation of organic matter mainly depends on the active species ·O<sub>2</sub><sup>-</sup>, ·OH, h<sup>+</sup>, and <sup>1</sup>O<sub>2</sub> (Shoneye and Tang 2020). Therefore, free radical capture experiments were used to determine the active species produced in photocatalytic reaction. TBA, TEMPOL, KI, and BQ were introduced to scavenge ·OH, <sup>1</sup>O<sub>2</sub>, h<sup>+</sup>, and ·O<sub>2</sub><sup>-</sup>, respectively. As shown in Fig. 6e, compared with the blank experiment, the degradation efficiency of TiO<sub>2</sub>/α-FeOOH was significantly inhibited when BQ, KI, or TEMPOL was added into the reaction system, indicating that ·O<sub>2</sub><sup>-</sup>, h<sup>+</sup>, and <sup>1</sup>O<sub>2</sub> are the main active species produced in degradation process for TiO<sub>2</sub>/α-FeOOH. The ESR characterization was used to further determine the main reactive species during the photocatalytic degradation process (Wang et al. 2018). As presented in Fig. 6f, the characteristic peaks were identified as the characteristic signature of DMPO-·O<sub>2</sub><sup>-</sup>, and there is a significant improvement in the generation of ·O<sub>2</sub><sup>-</sup> for TiO<sub>2</sub>/α-FeOOH. From Fig. 6g, it can be found that the appearance of three signals corresponds to the signal of h<sup>+</sup>. As we know, the weaker the ESR signal, the more h<sup>+</sup> is produced (Xu et al. 2023); therefore, the yield of h<sup>+</sup> by TiO<sub>2</sub>/α-FeOOH is significantly higher than that of α-FeOOH but equivalent to TiO<sub>2</sub>. Moreover, the weak triple signals of TEMP-<sup>1</sup>O<sub>2</sub> were detected in Fig. 6h. These observations suggest that ·O<sub>2</sub><sup>-</sup>, h<sup>+</sup>, and <sup>1</sup>O<sub>2</sub> free radicals are produced by TiO<sub>2</sub>/α-FeOOH, which is consistent with the free radical capture experiments.

Based on the above experimental results, the possible photocatalytic mechanism of TiO<sub>2</sub>/α-FeOOH was proposed. When TiO<sub>2</sub>/α-FeOOH is exposed to simulated sunlight, the valence band electrons of TiO<sub>2</sub> and α-FeOOH are excited to transfer to the conduction band and leave holes in the valence band. When the conduction band potential is less

than O<sub>2</sub>/·O<sub>2</sub><sup>-</sup> (-0.33 V vs NHE), O<sub>2</sub> can obtain electron to generate ·O<sub>2</sub><sup>-</sup>. Because the conduction band potential of TiO<sub>2</sub> is not enough to reduce O<sub>2</sub> to generate ·O<sub>2</sub><sup>-</sup>; therefore, the ESR detection showed that ·O<sub>2</sub><sup>-</sup> is not the main active species produced by TiO<sub>2</sub>. For α-FeOOH, the conduction band potential is -0.61 V, which can reduce O<sub>2</sub> to ·O<sub>2</sub><sup>-</sup>. Importantly, it can be seen from Fig. 6g that the characteristic peak of ·O<sub>2</sub><sup>-</sup> is significantly improved after a combination between TiO<sub>2</sub> and α-FeOOH. Therefore, it can be speculated that TiO<sub>2</sub> and α-FeOOH are not simple type II heterojunction structure, but actually form a Z-type electron transfer structure (Qi et al. 2017; Yu et al. 2022). The combination of conduction band electrons of TiO<sub>2</sub> with valence band h<sup>+</sup> of α-FeOOH valence band h<sup>+</sup> inhibits the recombination of photogenerated electrons and holes, leading to the electrons in conduction band of α-FeOOH and holes in valence band of TiO<sub>2</sub> are left and have high redox capacity, respectively (Meng et al. 2013; Sun et al. 2023). The above results indicate that the enhanced photocatalytic activity of TiO<sub>2</sub>/α-FeOOH is mainly due to the matching relative band potential, which enhances the electron transfer ability and reduces the recombination of electron-hole pairs of the composite system (Yan et al. 2023).

### Proposed degradation products and pathway of fluoranthene

The photocatalytic degradation products of fluoranthene were identified by GC-MS, and the intermediate information based on this study (red) and literatures was presented in Table S4. The possible degradation pathway during photocatalytic reaction was proposed and shown in Fig. 7. In the photocatalytic reaction system of TiO<sub>2</sub>/α-FeOOH heterojunction, the oxidation reaction of fluoranthene was probably initiated from the attack at aromatic ring positions by oxidizing radicals, resulting in the formation of aromatic alcohol fluoranthene-1,2-diol (Product 1, m/z = 234) through electron transfer and hydroxylation (Bai et al. 2019). Through ketonizing, product 1 was further turned to be 3,10b-dihydrofluoranthene-1,2-dione (product 2 m/z = 234). Subsequently, an

**Table 1** Comparison of various technical system on degradation of pollutants in soil

Catalyst	Dosage	Target pollutants	Concentration	Reaction time	Degradation (%)	Ref
Fe <sub>3</sub> O <sub>4</sub> @NaBC@GA@LC	50 mg/g	5-rings PAHs	–	40 d	91.36%	(Zheng et al. 2023)
TiO <sub>2</sub>	20 mg/g	Phenanthrene and pyrene	40 mg/kg	25 h	38.7%	(Dong et al. 2010a)
FeOOH + PMS	10 mg/g	PAHs	–	7 d	84.8%	(Tang et al. 2023)
Fe <sub>2</sub> O <sub>3</sub>	5 g/m <sup>2</sup>	Pyrene	20 mg/g	12 h	21%	(Wang et al. 2009)
TiO <sub>2</sub>	150 mg/g	Dioxin	11.7 ppb	120 d	79.6%	(Binh et al. 2013)
TiO <sub>2</sub> @ZnHCF	30 mg/g	Phenanthrene	2 mg/L	24 h	84%	(Rachna et al. 2019)
TiO <sub>2</sub> /α-FeOOH	10 mg/g	Fluoranthene	40 mg/kg	24 h	60%	This study

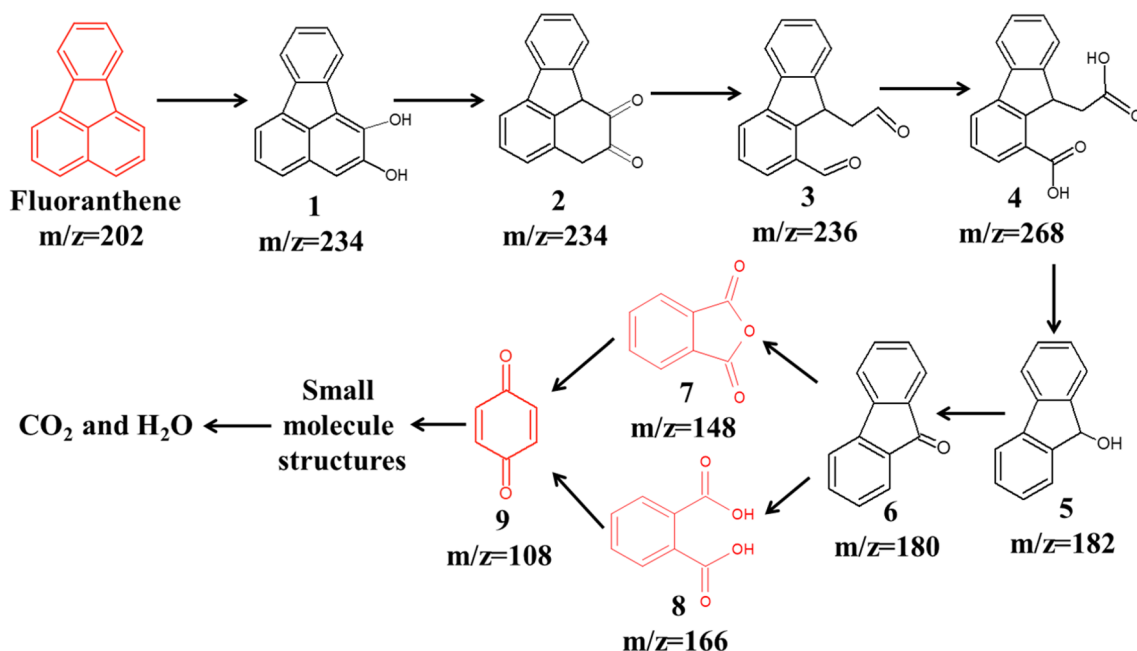


**Fig. 7** Potential photocatalytic degradation pathways of fluoranthene

open loop reaction, losing oxalic acid, and hydroxylation occurred, which led to the formation of 9-(2-oxoethyl)-9H-fluorene-1-carbaldehyde (product 3  $m/z = 236$ ). Further oxidation of product 3 resulted in the generation of 9-(carboxymethyl)-9H-fluorene-1-carboxylic acid (product 4  $m/z = 268$ ). Then, the 9-hydroxyfluorene (Product 5  $m/z = 182$ ) was formed by further decarboxylation and hydroxyl substitution. Further oxidation by ketonizing generates the 9-fluorenone (product 6  $m/z = 180$ ). Attack of active radicals on 9-fluorenone resulted in the formation of phthalic anhydride (product 7  $m/z = 148$ ) and phthalic acid (product 8  $m/z = 166$ ) by cracking ring, hydroxylation, and oxidation. Finally, 1,4-naphthoquinone (product 9  $m/z = 108$ ) was formed through loss of CO and tautomerism (Theerakarunwong et al. 2018). These products will be further photocatalytic oxidation to small molecular organic compounds,  $\text{CO}_2$ , and  $\text{H}_2\text{O}$ .

## Conclusion

In this work,  $\text{TiO}_2/\alpha\text{-FeOOH}$  photocatalyst was prepared by hydrothermal method and sol-gel method. SEM, TEM, XRD, XPS, EDS, Raman, and FTIR spectroscopy measurements indicated that  $\text{TiO}_2/\alpha\text{-FeOOH}$  has been successfully constructed. The combination of  $\text{TiO}_2$  and  $\alpha\text{-FeOOH}$  obviously improved the optical absorption capacity compared with  $\text{TiO}_2$  in the visible region, and increased the separation efficiency of electrons and holes. The  $\text{TiO}_2/\alpha\text{-FeOOH}$  showed greatly enhanced photocatalytic

performance and had good reaction stability. The photocatalytic degradation system of soil suspension enhanced the light transmission and improved the degradation efficiency. Under a water/soil ratio of 10:1, a photocatalyst dosage of 50 mg/g, and an initial pH of 6,  $\text{TiO}_2/\alpha\text{-FeOOH}$  had the best degradation efficiency on fluoranthene, clearly outperforming both  $\text{TiO}_2$  and  $\alpha\text{-FeOOH}$ . The primary active species generated during the degrading process of  $\text{TiO}_2/\alpha\text{-FeOOH}$  were  $\cdot\text{O}_2^-$ ,  $\text{h}^+$ , and  $^1\text{O}_2$ . Results showed that  $\text{TiO}_2/\alpha\text{-FeOOH}$  improves photocatalytic performance by forming a Z-type electron transfer structure and providing more redox active free radicals. Three degradation products were detected, and the degradation pathways were proposed.

**Supplementary Information** The online version contains supplementary material available at <https://doi.org/10.1007/s11356-024-32501-z>.

**Author contribution** Bingjie Yin: methodology, data curation, investigation, writing-original draft, and visualization. Jingying Li: data curation, validation, and investigation. Wei Guo: formal analysis and software. Haoqing Dong: validation and formal analysis. Guangshan Zhang: methodology. Yanjun Xin: writing—review and editing. Guodong Zhang: methodology, writing—review and editing. Qinghua Chen: conceptualization, funding acquisition, formal analysis, data curation, supervision, methodology, resources, writing—review and editing.

**Funding** This work was supported by the Support Plan on Youth Innovation Science and Technology for Higher Education of Shandong Province (no. 2019KJD014), Natural Science Foundation of Shandong Province (no. ZR2019MD012), National Natural Science Foundation of China (no. 52070107), Science & Technology Specific Projects in Agricultural High-tech Industrial Demonstration Area

of the Yellow River Delta (grant no: 2022SZX35), and Special Project of Qingdao Science and Technology Benefiting the People (no. 23–2-8-cspz-1-nsh).

**Data availability** The data that support the findings of this study are available from the corresponding author upon reasonable request.

## Declarations

**Ethical approval.** Not applicable.

**Consent to participate** Not applicable.

**Consent for publication** Not applicable.

**Competing interests** The authors declare no competing interests.

## References

- Anju S, Yesodharan S, Yesodharan E (2012) Zinc oxide mediated sonophotocatalytic degradation of phenol in water. *Chem Eng J* 189–190:84–93
- Bai X, Wang Y, Zheng X, Zhu K, Long A, Wu X, Zhang H (2019) Remediation of phenanthrene contaminated soil by coupling soil washing with Tween 80, oxidation using the UV/S<sub>2</sub>O<sub>8</sub><sup>2-</sup> process and recycling of the surfactant. *Chem Eng J* 369:1014–1023
- Bang J, Kamat P (2010) Solar cells by design: photoelectrochemistry of TiO<sub>2</sub> nanorod arrays decorated with CdSe. *Adv Funct Mater* 20:1970–1976
- Binh N, Oanh N, Parkpian P (2013) Photodegradation of dioxin in contaminated soil in the presence of solvents and nanoscale TiO<sub>2</sub> particles. *Environ Technol* 35:1121–1132
- Bisquert J, Zaban A, Greenshtein M, Mora-Sero I (2004) Determination of rate constants for charge transfer and the distribution of semiconductor and electrolyte electronic energy levels in dye-sensitized solar cells by open-circuit photovoltage decay method. *J Am Chem Soc* 126:13550–13559
- Bisquert J, Fabregat-Santiago F, Mora-Seró I, Garcia-Belmonte G, Giménez S (2009) Electron Lifetime in Dye-Sensitized solar Cells: Theory and Interpretation of Measurements. *J Phys Chem C* 113:17278–17290
- Cao S, Liu T, Tsang Y, Chen C (2016) Role of hydroxylation modification on the structure and property of reduced graphene oxide/TiO<sub>2</sub> hybrids. *Appl Surf Sci* 382:225–238
- Chen Q, Wu S, Xin Y (2016) Synthesis of Au-CuS-TiO<sub>2</sub> nanobelts photocatalyst for efficient photocatalytic degradation of antibiotic oxytetracycline. *Chem Eng J* 302:377–387
- Cizmar T, Kojic V, Rukavina M, Brkljacic L, Salamon K, Grcic I, Radetic L, Gajovic A (2020) Hydrothermal synthesis of FeOOH and Fe<sub>2</sub>O<sub>3</sub> modified self-organizing immobilized TiO<sub>2</sub> nanotubes for photocatalytic degradation of 1H-benzotriazole. *Catalysts* 10:1371
- Dong D, Li P, Li X, Xu C, Gong D, Zhang Y, Zhao Q, Li P (2010a) Photocatalytic degradation of phenanthrene and pyrene on soil surfaces in the presence of nanometer rutile TiO<sub>2</sub> under UV-irradiation. *Chem Eng J* 158:378–383
- Dong D, Li P, Li X, Zhao Q, Zhang Y, Jia C, Li P (2010b) Investigation on the photocatalytic degradation of pyrene on soil surfaces using nanometer anatase TiO<sub>2</sub> under UV irradiation. *J Haz Mat* 174:859–863
- Du J, Liu J, Jia T, Chai B (2022) The relationships between soil physicochemical properties, bacterial communities and polycyclic aromatic hydrocarbon concentrations in soils proximal to coking plants. *Environ Pollut* 298:118823
- Guo Y, Li C, Gong Z, Guo Y, Wang X, Gao B, Qin W, Wang G (2020) Photocatalytic decontamination of tetracycline and Cr (VI) by a novel alpha-FeOOH/FeS<sub>2</sub> photocatalyst: one-pot hydrothermal synthesis and Z-scheme reaction mechanism insight. *J Hazard Mater* 397:122580
- Gupta V, Jain R, Mittal A, Saleh T, Nayak A, Agarwal S, Sikarwar S (2012) Photo-catalytic degradation of toxic dye amaranth on TiO<sub>2</sub>/UV in aqueous suspensions. *Mat Sci Eng C-Mater* 32:12–17
- Huang Y, Gao Y, Zhang Q, Zhang Y, Cao J, Ho W, Lee S (2018) Biocompatible FeOOH-carbon quantum dots nanocomposites for gaseous NO<sub>x</sub> removal under visible light: improved charge separation and high selectivity. *J Haz Mat* 354:54–62
- Jaffari Z, Lam S, Sin J, Zeng H, Mohamed A (2020) Magnetically recoverable Pd-loaded BiFeO<sub>3</sub> microcomposite with enhanced visible light photocatalytic performance for pollutant, bacterial and fungal elimination. *Sep Purif Technol* 236:116195
- Jaffari Z, Abuabdou S, Ng D, Bashir M (2021) Insight into two-dimensional MXenes for environmental applications: recent progress, challenges, and prospects. *FlatChem* 28:100256
- Kariyawasam T, Doran G, Howitt J, Prenzler P (2022) Polycyclic aromatic hydrocarbon contamination in soils and sediments: sustainable approaches for extraction and remediation. *Chemosphere* 291:132981
- Lam S, Jaffari Z, Sin J, Zeng H, Lin H, Li H, Mohamed A, Ng D (2021) Surface decorated coral-like magnetic BiFeO<sub>3</sub> with Au nanoparticles for effective sunlight photodegradation of 2,4-D and E. coli inactivation. *J Mol Liq* 326:115372
- Lam S, Choong M, Sin J, Zeng H, Huang L, Hua L, Li H, Jaffari Z, Cho K (2022) Construction of delaminated Ti<sub>3</sub>C<sub>2</sub> MXene/NiFe<sub>2</sub>O<sub>4</sub>/V<sub>2</sub>O<sub>5</sub> ternary composites for expeditious pollutant degradation and bactericidal property. *J Environ Chem Eng* 10:108284
- Li X, Huang Y, Li C, Shen J, Deng Y (2015) Degradation of pCNB by Fenton-like process using α-FeOOH. *Chem Eng J* 260:28–36
- Liang Q, Cui S, Liu C, Xu S, Yao C, Li Z (2018) Construction of CdS@UIO-66-NH<sub>2</sub> core-shell nanorods for enhanced photocatalytic activity with excellent photostability. *J Colloid Interf Sci* 524:379–387
- Lin F, Yuan M, Chen Y, Huang Y, Cao S (2019) Advanced asymmetric supercapacitor based on molybdenum trioxide decorated nickel cobalt oxide nanosheets and three-dimensional α-FeOOH/rGO. *Electrochim Acta* 320:134580
- Liu Y, Liu X, Zhao Y, Dionysiou D (2017) Aligned α-FeOOH nanorods anchored on a graphene oxide-carbon nanotubes aerogel can serve as an effective Fenton-like oxidation catalyst. *Appl Catal b: Environ* 213:74–86
- Liu J, Wei K, Xu S, Cui J, He X (2021) Surfactant-enhanced remediation of oil-contaminated soil and groundwater: a review. *Sci Total Environ* 756:144142
- Ma D, Shi J, Zou Y, Fan Z, Ji X, Niu C (2017) Highly efficient photocatalyst based on a CdS quantum Dots/ZnO nanosheets 0D/2D heterojunction for hydrogen evolution from water splitting. *ACS Appl Mater Interfaces* 9:25377–25386
- Ma X, Chen Q, Liu G, Zhou Y, Ma D, Xin S, Yu C, Zhang B, Xin Y (2020) Construction of netlike 3D Z-scheme photoelectrodes with improved photocatalytic performance based on g-C<sub>3</sub>N<sub>4</sub> nanosheets modified TiO<sub>2</sub> nanobelt-tubes. *Chem Eng Sci* 226:115844
- Magalhães A, Nunes D, Robles-Dutenhefner P, De Sousa E (2004) Catalytic activity of porous TiO<sub>2</sub> obtained by sol-gel process in the degradation of phenol. *J Non-Cryst Solids* 348:185–189
- Meekins B, Kamat P (2009) Got TiO<sub>2</sub> nanotubes? Lithium ion intercalation can boost their photoelectrochemical performance. *ACS Nano* 3:3437–3446
- Meng F, Li J, Cushing S, Bright J, Zhi M, Rowley J, Hong Z, Manivannan A, Bristow A, Wu N (2013) Photocatalytic water

- oxidation by hematite/reduced graphene oxide composites. *ACS Catal* 3:746–751
- Mor G, Shankar K, Paulose M, Varghese O, Grimes C (2013) Use of highly-ordered TiO<sub>2</sub> nanotube arrays in dye-sensitized solar cells. *Nano Lett* 6:215–218
- Pant B, Park M, Park S (2019) TiO<sub>2</sub> NPs Assembled into a carbon nanofiber composite electrode by a one-step electrospinning process for supercapacitor applications. *Polymers* 11:899
- Qi K, Cheng B, Yu J, Ho W (2017) A review on TiO<sub>2</sub> based Z-scheme photocatalysts. *Chinese J Catal* 38:1936–1955
- Qian X, Ren M, Zhu Y, Yue D, Han Y, Jia J, Zhao Y (2017) Visible light assisted heterogeneous Fenton-like degradation of Irganic pollutant via  $\alpha$ -FeOOH/mesoporous carbon composites. *Environ Sci Technol* 51:3993–4000
- Rachna R, Shanker U (2019) Degradation of tricyclic polyaromatic hydrocarbons in water, soil and river sediment with a novel TiO<sub>2</sub> based heterogeneous nanocomposite. *J Environ Manage* 248:109340
- Rahimi S, Moattari R, Rajabi L, Derakhshan A, Keyhani M (2015) Iron oxide/hydroxide ( $\alpha$ ,  $\gamma$ -FeOOH) nanoparticles as high potential adsorbents for lead removal from polluted aquatic media. *J Ind Eng Chem* 23:33–43
- Rajender G, Kumar J, Giri P (2018) Interfacial charge transfer in oxygen deficient TiO<sub>2</sub>-graphene quantum dot hybrid and its influence on the enhanced visible light photocatalysis. *Appl Catal b: Environ* 224:960–972
- Sahnesarayi M, Sarpoolaky H, Rastegari S (2014) Effect of heat treatment temperature on the performance of nano-TiO<sub>2</sub> coating in protecting 316L stainless steel against corrosion under UV illumination and dark conditions. *Surf Coat Tech* 258:861–870
- Sajjadizadeh H, Goharshadi E, Ahmadzadeh H (2019) Photoelectrochemical water splitting by engineered multilayer TiO<sub>2</sub>/GQDs photoanode with cascade charge transfer structure. *Int J Hydrogen Energ* 45:123–134
- Saravanan A, Deivayanai V, Kumar P, Rangasamy G, Hemavathy R, Harshana T, Gayathri N, Alagumalai K (2022) A detailed review on advanced oxidation process in treatment of wastewater: mechanism, challenges and future outlook. *Chemosphere* 308:136524
- Shoneye A, Tang J (2020) Highly dispersed FeOOH to enhance photocatalytic activity of TiO<sub>2</sub> for complete mineralisation of herbicides. *Appl Surf Sci* 511:145479.1–145479.11
- Sultan M, Miyazaki T, Koyama S (2018) Optimization of adsorption isotherm types for desiccant air-conditioning applications. *Renew Energ* 121:441–450
- Sun L, Feng Y, Ma K, Jiang X, Gao Z, Wang J, Jiang N, Liu X (2022) Synergistic effect of single-atom Ag and hierarchical tremella-like g-C<sub>3</sub>N<sub>4</sub>: electronic structure regulation and multi-channel carriers transport for boosting photocatalytic performance. *Appl Catal b: Environ* 306:121106
- Sun F, Xie Y, Xu D, Liu F, Qi H, Ma Q, Yang Y, Yu H, Yu W, Dong X (2023) Electrospun self-supporting double Z-scheme tricolor-typed microfiber oriented-heterostructure photocatalyst with highly effective hydrogen evolution and organic pollutants degradation. *J Environ Chem Eng* 11:109169
- Tang X, Guo J, Gao Y, Zhen K, Sun H, Wang C (2023) Efficient remediation of the field soil contaminated with PAHs by amorphous porous iron material activated peroxy monosulfate. *Chemosphere* 327:138516
- Theerakarunwong C, Phanichphant S (2018) Visible-light-induced photocatalytic degradation of PAH-contaminated soil and their pathways by Fe-doped TiO<sub>2</sub> nanocatalyst. *Water Air Soil Pollut* 229:291
- Wang Y, Liu C, Li F, Liu C, Liang J (2009) Photodegradation of polycyclic aromatic hydrocarbon pyrene by iron oxide in solid phase. *J Hazard Mater* 162:716–723
- Wang A, Teng Y, Hu X, Wang L, Huang Y, Luo Y, Christie P (2016) Diphenylarsinic acid contaminated soil remediation by titanium dioxide (P25) photocatalysis: degradation pathway, optimization of operating parameters and effects of soil properties. *Sci Total Environ* 541:348–355
- Wang Y, Fang J, Crittenden J, Shen C (2017) Novel RGO/ $\alpha$ -FeOOH supported catalyst for Fenton oxidation of phenol at a wide pH range using solar-light-driven irradiation. *J Hazard Mater* 329:321–329
- Wang F, Feng Y, Zeng Y, Xie Y, Zhang Z (2018) Novel ternary photocatalyst of single atom-dispersed silver and carbon quantum dots co-loaded with ultrathin g-C<sub>3</sub>N<sub>4</sub> for broad spectrum photocatalytic degradation of naproxen. *Appl Catal b: Environ* 221:510–520
- Wang J, Wang B, Shi W, Qiao X, Yang X, Zhang L, Zhang W, Li R, Hou Y (2022) Natural-sunlight-driven synchronous degradation of 4-nitrophenol and rhodamine B over S-scheme heterojunction of  $\alpha$ -Fe<sub>2</sub>O<sub>3</sub> nanoparticles decorated CuBi<sub>2</sub>O<sub>4</sub> rods. *J Environ Chem Eng* 10:108565
- Wei Y, Ding R, Zhang C, Lv B, Wang Y, Chen C, Wang X, Xu J, Yang Y, Li Y (2017) Facile synthesis of self-assembled ultrathin  $\alpha$ -FeOOH nanorod/graphene oxide composites for supercapacitors. *J Colloid Interface Sci* 504:593–602
- Wu C, Liu Q, Zhan Y, Tan W, Wei X, Tong Q, Wan H, Dong L (2023) Insights into the surface structure-sensitive photocatalytic oxidation of gaseous toluene on Pd/TiO<sub>2</sub> catalysts. *Chem Eng J* 475:146294
- Xie W, Chen H, Zhang X, Hu X, Li G (2013) Preparation and photocatalytic activity of rutile TiO<sub>2</sub> and goethite composite photocatalysts. *Chinese J Catal* 34:1076–1086
- Xu Y, Schoonen M (2000) The absolute energy positions of conduction and valence bands of selected semiconducting minerals. *AM Mineral* 85:543–556
- Xu C, Li D, Liu H, Wang D, Liu X, Lin S, Yang Y, Fan D, Pan H (2023) Construction of 1D/0D CdS nanorods/Ti<sub>3</sub>C<sub>2</sub> QDs Schottky heterojunctions for efficient photocatalysis. *J Environ Chem Eng* 11:109191
- Yan Q, Guo Z, Wang P, Cheng Y, Wu C, Zuo H (2023) Facile construction of 0D/2D In<sub>2</sub>O<sub>3</sub>/Bi<sub>2</sub>WO<sub>6</sub> Z-scheme heterojunction with enhanced photocatalytic activity for antibiotics removal. *J Alloys Compd* 937:168362
- Yang G, Jiang Y, Yin B, Liu G, Ma D, Zhang G, Zhang G, Xin Y, Chen Q (2023) Efficiency and mechanism on photocatalytic degradation of fluoranthene in soil by Z-scheme g-C<sub>3</sub>N<sub>4</sub>/ $\alpha$ -Fe<sub>2</sub>O<sub>3</sub> photocatalyst under simulated sunlight. *Environ Sci Pollut R* 30:70260–70276
- Yong Z, Lam S, Sin J, Zeng H, Mohamed A, Jaffari Z (2022) Boosting sunlight-powered photocatalytic fuel cell with S-scheme Bi<sub>2</sub>WO<sub>6</sub>/ZnO nanorod array composite photoanode. *Inorg Chem Commun* 143:109826
- Yu H, Zhang S, Zhao H, Will G, Liu P (2009) An efficient and low-cost TiO<sub>2</sub> compact layer for performance improvement of dye-sensitized solar cells. *Electrochim Acta* 54:1319–1324
- Yu Q, Dai Y, Ling Y, Wu Q, Zhang Z, Feng B (2022) Z-scheme heterojunction WO<sub>3</sub>/BiOBr supported-single Fe atom for ciprofloxacin degradation via visible-light photocatalysis. *J Environ Chem Eng* 10:108693
- Zhang X, Niu Y, Meng X, Li Y, Zhao J (2013) Structural evolution and characteristics of the phase transformations between  $\alpha$ -Fe<sub>2</sub>O<sub>3</sub>, Fe<sub>3</sub>O<sub>4</sub> and  $\gamma$ -Fe<sub>2</sub>O<sub>3</sub> nanoparticles under reducing and oxidizing atmospheres. *CrystEngComm* 15:8166–8172
- Zhang Y, Sui X, Zhao L, Gu D, Huang G, Wang Z (2019) Controlling the surface roughness of chain-like Pd nanowires by pH values as excellent catalysts for oxygen reduction reaction. *Int J Hydrogen Energ* 44:6551–6559
- Zhang B, Ma X, Ma J, Zhou Y, Liu C, Deng Z, Luo M, Xin Y (2020) Fabrication of rGO and g-C<sub>3</sub>N<sub>4</sub> co-modified TiO<sub>2</sub> nanotube arrays

- photoelectrodes with enhanced photocatalytic performance. *J Colloid Interf Sci* 577:75–85
- Zhang C, Xiong W, Li Y, Lin L, Zhou X, Xiong X (2023) Continuous inactivation of human adenoviruses in water by a novel g-C<sub>3</sub>N<sub>4</sub>/WO<sub>3</sub>/biochar memory photocatalyst under light-dark cycles. *J Hazard Mater* 442:130031
- Zhao X, Quan X, Chen S, Zhao H, Liu Y (2007) Photocatalytic remediation of  $\gamma$ -hexachlorocyclohexane contaminated soils using TiO<sub>2</sub> and montmorillonite composite photocatalyst. *J Environ Sci* 019:358–361
- Zhao H, Cui S, Yang L, Li G, Li N, Li X (2018) Synthesis of hierarchically meso-macroporous TiO<sub>2</sub>/CdS heterojunction photocatalysts with excellent visible-light photocatalytic activity. *J Colloid Interf Sci* 512:47–54
- Zheng X, Liu X, Wang W, Wang X, Zhang Z (2015) Enhanced photoelectrochemical and photocatalytic performance of TiO<sub>2</sub> nanorod arrays/CdS quantum dots by coating TiO<sub>2</sub> through atomic layer deposition. *Nano Energy* 11:400–408
- Zheng Z, Liu W, Zhou Q, Li J, Ze A, Wang Q, Lian Y, Shi R, Wang J (2023) Effects of co-modified biochar immobilized laccase on remediation and bacterial community of PAHs-contaminated soil. *J Hazard Mater* 443:130372

**Publisher's Note** Springer Nature remains neutral with regard to jurisdictional claims in published maps and institutional affiliations.

Springer Nature or its licensor (e.g. a society or other partner) holds exclusive rights to this article under a publishing agreement with the author(s) or other rightsholder(s); author self-archiving of the accepted manuscript version of this article is solely governed by the terms of such publishing agreement and applicable law.